

Structural stability and mechanical properties of TiB_6: A CALYPSO-guided exploration for superhard applications

Bo Sun(孙博), Yutong Zou(邹雨桐), Tao Wang(王淘), Yujia Wang(王雨佳), Jinyu Liu(刘金禹), Lili Gao(高丽丽), Meiguang Zhang(张美光), and Miao Zhang(张淼)

Citation: Chin. Phys. B, 2026, 35 (**5**): 056105. DOI: 10.1088/1674-1056/adfb59
http://cpb.iphy.ac.cn; http://iopscience.iop.org/cpb

What follows is a list of articles you may be interested in

Elasticity of quasi-bcc ammonia hemihydrate at high pressures

Mengqiong Pu(蒲梦琼), Jiacheng Zhang(张家诚), Xinyang Li(李新阳), Xiaomei Yuan(苑晓美), Xue Zhang(张雪), Shuo Gao(高硕), Chenlu Wang(王晨璐), Liang Li(李亮), Fangfei Li(李芳菲), and Qiang Zhou(周强)

Chin. Phys. B, 2026, 35 (**3**): 036101. DOI: 10.1088/1674-1056/ae330a

Synergistic improvements in mechanical and thermal performance of TiB_2 solid-solution-based composites

Zhuang Li(李壮), Cun You(由存), Zhihui Li(李志慧), Xuepeng Li(李雪鹏), Guiqian Sun(孙贵乾), Xinglin Wang(王星淋), Qi Jia(贾琪), Qiang Tao(陶强), and Pinwen Zhu(朱品文)

Chin. Phys. B, 2025, 34 (**8**): 086105. DOI: 10.1088/1674-1056/add00c

Heterogeneous TiC-based composite ceramics with high toughness

Xiaoci Ma(马孝慈), Yufei Ge(葛雨非), Yutong Hou(侯语同), Keyu Shi(施柯羽), Jiaqi Zhang(张佳琪), Gaoping Yue(岳高平), Qiang Tao(陶强), and Pinwen Zhu(朱品文)

Chin. Phys. B, 2025, 34 (**8**): 086104. DOI: 10.1088/1674-1056/add5c8

Morphology-tuned phase transition of MnO_2 nanorods under high pressure

Xue-Ting Zhang(张雪婷), Chen-Yi Li(李晨一), Hui Tian(田辉), Xin-Yue Wang(王心悦), Zong-Lun Li(李宗伦), and Quan-Jun Li(李全军)

Chin. Phys. B, 2025, 34 (**6**): 066105. DOI: 10.1088/1674-1056/adc192

Layer-dependent structural stability and electronic properties of $CrPS_4$ under high pressure

Jian Zhu(朱健), Dengman Feng(冯登满), Liangyu Wang(王亮予), Liang Li(李亮), Fangfei Li(李芳菲), Qiang Zhou(周强), and Yalan Yan(闫雅兰)

Chin. Phys. B, 2025, 34 (**6**): 066102. DOI: 10.1088/1674-1056/adc65f

---

SPECIAL TOPIC — John Tse: Pioneer in high-pressure materials science

Structural stability and mechanical properties of TiB_6: A CALYPSO-guided exploration for superhard applications

Bo Sun(孙博)[1], Yutong Zou(邹雨桐)[1], Tao Wang(王淘)[1], Yujia Wang(王雨佳)[1], Jinyu Liu(刘金禹)[1], Lili Gao(高丽丽)[1], Meiguang Zhang(张美光)[2,†], and Miao Zhang(张淼)[1,‡]

[1] *Department of Physics, School of Sciences, Beihua University, Jilin* 132013, *China*
[2] *College of Physics and Optoelectronic Technology, Baoji University of Arts and Sciences, Baoji* 721016, *China*

(Received 15 June 2025; revised manuscript received 20 July 2025; accepted manuscript online 14 August 2025)

Titanium–boron (Ti–B) compounds exhibit great promise as superhard materials due to titanium's low atomic mass and abundant valence electrons. In this work, we systematically investigated the crystal structures of TiB_6 under pressures ranging from 0–100 GPa using the CALYPSO algorithm combined with first-principles calculations. Phonon dispersion analysis and elastic-constant evaluations confirm the dynamic and mechanical stability of five predicted TiB_6 structures. Notably, the α-*Amm*2-TiB_6 structure was predicted to have a remarkable Vickers hardness of 56 GPa, as estimated by Chen's empirical model. All five structures are thermodynamically stable under ambient conditions, suggesting viable synthetic pathways. Their outstanding bulk moduli and ultrahigh hardness further classify them as potential incompressible and superhard materials. These theoretical insights lay a robust foundation for future experimental synthesis efforts.

Keywords: superhard materials, transition metal borides, Vickers hardness, first-principles calculations, CALYPSO method

PACS: 61.50.Ah, 61.50.Ks, 61.66.Fn

DOI: 10.1088/1674-1056/adfb59 **CSTR:** 32038.14.CPB.adfb59

1. Introduction

Superhard materials are extensively utilized in mechanical processing, aerospace, and various related areas owing to their exceptional mechanical properties.[1–3] The investigation of superhard materials exhibiting excellent properties is of fundamental significance for the advancement of condensed matter physics. Beyond the conventional superhard materials, such as diamond,[4] BC_3,[5,6] *c*-BN,[7] and C_3N_2,[8] transition metal borides (TMBs) have attracted substantial interest on account of their high valence electron density and robust covalent bonds, superior wear resistance, and excellent oxidation resistance. These characteristics render them exceptional candidates for the development of new superhard materials.[9,10]

To date, a number of TMBs have been experimentally synthesized or theoretically predicted.[11–25] For example, ReB_2 was synthesized at ambient pressure with a Vickers hardness of 48 GPa.[11] *Pnnm*-CrB_4 has been identified as a candidate for superhard materials, with its estimated Vickers hardness reaching 48 GPa.[12] Nevertheless, the experimentally measured Vickers hardness is only 23.3 GPa.[26] Both phases of WB_4 exhibit a high bulk modulus, a high shear modulus, and a low Poisson's ratio, making WB_4 a promising material with low compressibility.[27] Moreover, WB_4 has demonstrated an outstanding combination of high strength and improved ductility under shear strain.[28] Recent theoretical investigations have indicated that ZrB_6 can be synthesized experimentally at moderate pressures, achieving a Vickers hardness > 40 GPa.[13] The recently predicted structure *C*2-HfB_6 is expected to exhibit a superhardness of up to 50 GPa, positioning it as a potential superhard material.[14] The *Amm*2-TaB_6 phase demonstrates a high bulk modulus and strong resistance to compression, with a Vickers hardness of 40.8 GPa.[15] Notably, most TMBs contain transition metal elements that are heavier than titanium. Due to its relatively lighter atomic mass and abundant valence electrons, titanium-based systems may facilitate synthesis. A variety of Ti–B compounds have been synthesized, including TiB, TiB_2, and Ti_3B_4.[29,30] In theoretical work, Ti_3B_4, Ti_2B_3, TiB_2, Ti_2B_5, TiB_3, TiB_4, and TiB_{12} have been identified as potential superhard materials,[31–36] exhibiting simulated hardness values ranging from 32.3 GPa to 53.3 GPa. In particular, *Amm*2-TiB_3 exhibits a hardness value of 51.6 GPa,[33] while *Cmcm*-TiB_4 demonstrates a hardness value of 53.3 GPa.[34] The remarkable hardness of TiB_3 and TiB_4 motivates systematic investigation of novel boron-rich Ti–B compounds as potential candidates for superhard materials.

Within this study, we comprehensively explore the crystal structure and properties of TiB_6 via the CALYPSO method combined with first-principles calculations. Utilizing Chen's model, we predict five novel phases: α-*Amm*2, β-*Amm*2,

†Corresponding author. E-mail: zhmgbj@126.com
‡Corresponding author. E-mail: zhangmiaolmc@126.com

© 2026 Chinese Physical Society and IOP Publishing Ltd. All rights, including for text and data mining, AI training, and similar technologies, are reserved.

$P2/m$, α-$P2_1/m$, and β-$P2_1/m$. Among the proposed structures, the Vickers hardness of α-*Amm*2-TiB_6 reaches 56 GPa, rendering it the hardest titanium-boron compound identified to date. Computational analyses indicate that the five structures exhibit both dynamical and thermodynamic stability at atmospheric pressure. This research contributes to the ongoing exploration of new superhard materials.

2. Methods

Density functional theory (DFT), implemented in the Vienna *ab initio* simulation package (VASP), was employed to conduct structural optimization and electronic structure calculations.[37,38] We explored the properties of TiB_6 in the pressure range of 0–100 GPa using the CALYPSO code,[39] which has been specifically designed to explore the potential energy surfaces of chemical systems and identify global minima.[40] The electron exchange–correlation interactions were described using the generalized gradient approximation (GGA) formulated by Perdew, Burke, and Ernzerhof (PBE).[41,42] The projector augmented-wave (PAW)[43] method was used to treat ion–electron interactions, explicitly considering the $2s^22p^1$ electrons of B atoms and the $3s^23p^64s^23d^2$ electrons of Ti atoms.[44] To ensure accuracy, a plane-wave energy cutoff of 800 eV was used. Furthermore, dense Monkhorst–Pack *k*-meshes[45] of $10\times16\times8$ for α-*Amm*2, $10\times16\times4$ for β-*Amm*2, $11\times17\times6$ for $P2/m$, $7\times18\times12$ for α-$P2_1/m$, and $17\times18\times5$ for β-$P2_1/m$ were used. Phonon dispersion curves were calculated using a supercell approach implemented in the PHONOPY code to assess dynamical stability.[46] Elastic constants were derived using the strain–stress method. Subsequently, bulk modulus, shear modulus, Young's modulus, and Poisson's ratio were computed via the Voigt–Reuss–Hill approximation. Vickers hardness values were evaluated using Chen's model[47] and Tian's model.[48]

3. Results and discussion

3.1. Structural properties

We employed the CALYPSO method combined with first-principles calculations to explore stable TiB_6 compounds. We propose two orthorhombic phases: α-*Amm*2 and β-*Amm*2, along with three monoclinic phases: $P2/m$, α-$P2_1/m$, and β-$P2_1/m$, as illustrated in Fig. 1. For α-*Amm*2-TiB_6 and β-*Amm*2-TiB_6, each Ti atom is surrounded by twelve neighboring B atoms. The B atoms form parallel hexagonal planes with misaligned stacking arrangements. The B–B bonds exhibit bond lengths ranging from 1.72 Å to 1.83 Å. Importantly, the shortest B–B bonds in the predicted α-*Amm*2-TiB_6 and β-*Amm*2-TiB_6 phases are substantially shorter than those observed in established hard materials such as OsB_2 (1.85 Å).[49] Ti atoms are located at the central positions of two six-membered boron rings, and these rings differ in the number of boron layers. The α-*Amm*2 structure contains three layers, while the β-*Amm*2 structure consists of five layers. $P2/m$, α-$P2_1/m$, and β-$P2_1/m$ exhibit layered stacking along the *b*-axis, and Ti atoms occupy similar central positions within boron frameworks. The B–B bonds exhibit bond lengths ranging from 1.53 Å to 1.78 Å. The lattice constants, cell volumes, and atomic positions of TiB_6 after relaxation are listed in Table S1.

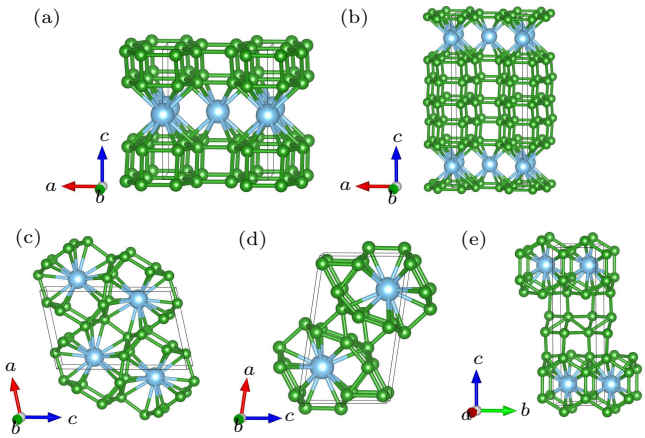


Fig. 1. Crystal structures of TiB_6. (a) α-*Amm*2, (b) β-*Amm*2, (c) $P2/m$, (d) α-$P2_1/m$, and (e) β-$P2_1/m$.

3.2. Phase stability

Here, we report the enthalpy differences of β-*Amm*2-TiB_6, $P2/m$-TiB_6, α-$P2_1/m$-TiB_6, and β-$P2_1/m$-TiB_6 relative to the α-*Amm*2-TiB_6 phase as a function of pressure. We also present information on metastable titanium borides at 0 GPa, 50 GPa, and 100 GPa. As shown in Fig. 2(a), the calculated enthalpy curves reveal the pressure ranges where different phases are thermodynamically stable. Up to 13 GPa, the α-$P2/m$ phase becomes more stable. When the pressure reaches 28 GPa, α-*Amm*2-TiB_6 becomes energetically favorable, and then transforms to β-*Amm*2- and β-$P2_1/m$-TiB_6 at 31 GPa and 62 GPa, respectively. Figures 2(b)–2(d) illustrate the thermodynamic convex hull of the Ti–B system, indicating that *Pnma*-TiB, $P6/mmm$-TiB_2,[50] and *Immm*-Ti_3B_4 are thermodynamically stable titanium borides at ambient pressure. The predicted TiB_6 compounds are metastable at ambient conditions. As shown in Figs. 2(b)–2(d), the formation enthalpy decreases with increasing pressure, reaching its minimum at 100 GPa. This suggests that the metastable TiB_6 phases may become stabilized under high pressure.

In order to demonstrate the dynamical stability of TiB_6, we assessed the lattice dynamics of the five structures by calculating their phonon spectra. Typically, the absence of imaginary phonon modes confirms dynamical stability.[51–53] As depicted in Fig. 3, the phonon dispersion relations of the TiB_6 compounds at atmospheric pressure exhibit no imaginary

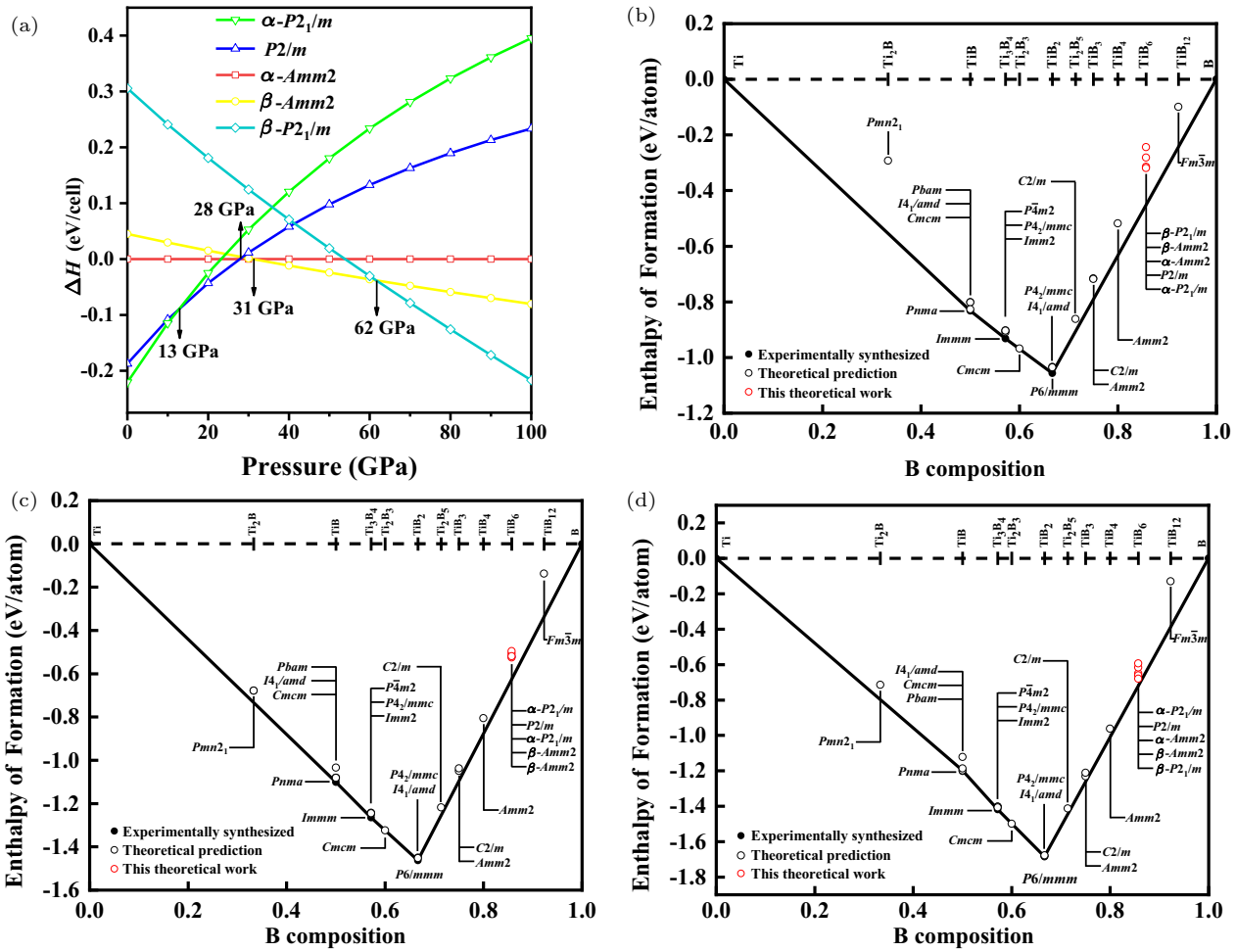


Fig. 2. (a) Enthalpy differences of β-*Amm*2-TiB_6, $P2/m$-TiB_6, α-$P2_1/m$-TiB_6, and β-$P2_1/m$-TiB_6 relative to α-*Amm*2-TiB_6 as a function of pressure. (b)–(d) Convex hull of the Ti–B system under (b) 0 GPa, (c) 50 GPa, and (d) 100 GPa.

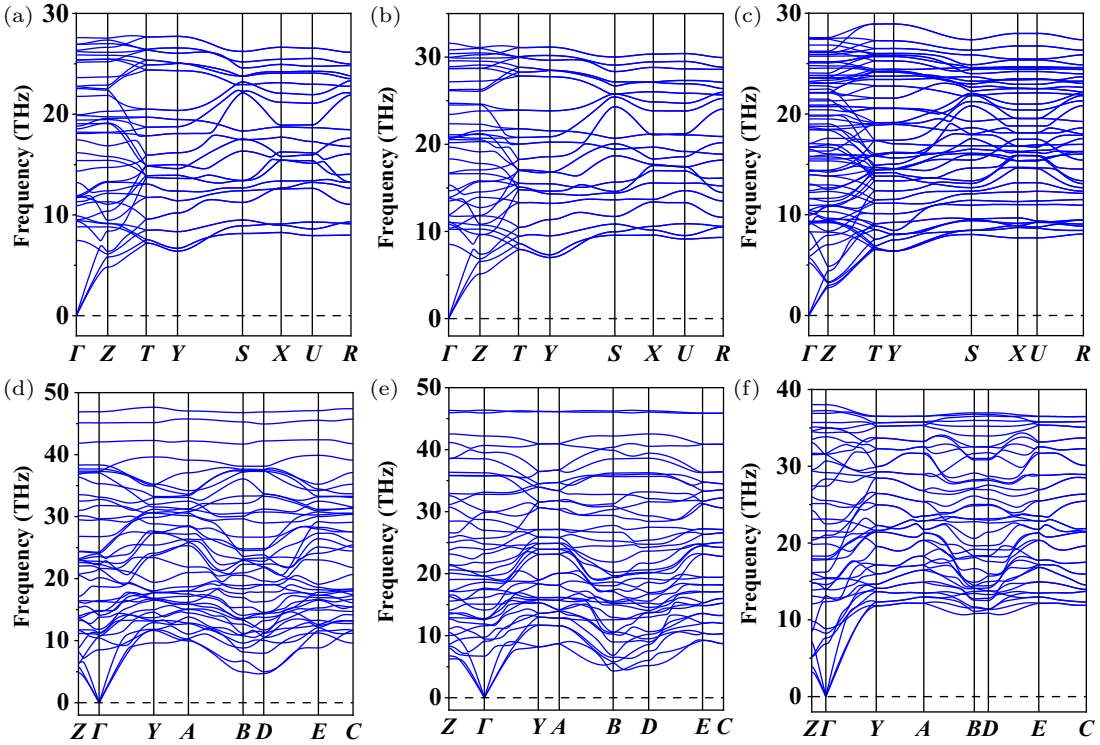


Fig. 3. Calculated phonon dispersion curves of TiB_6. (a) α-*Amm*2 at 0 GPa, (b) α-*Amm*2 at 30 GPa, (c) β-*Amm*2 at 0 GPa, (d) $P2/m$ at 0 GPa, (e) α-$P2_1/m$ at 0 GPa, and (f) β-$P2_1/m$ at 0 GPa.

frequencies within the Brillouin zone. Notably, the α-*Amm*2 phase maintains a stable phonon spectrum even at 30 GPa, which coincides with its thermodynamic stability range (28–31 GPa). These results confirm that all predicted TiB_6 structures are dynamically stable under ambient pressure conditions.

To evaluate the thermodynamic stability of the TiB_6 phases, we systematically determined the pressure-dependent formation enthalpies through four distinct synthetic pathways, as illustrated in Figs. 4 and S1. In the range of 0–100 GPa, with increasing pressure, the formation enthalpy becomes more negative, indicating that pressure enhances structural stability. The formation enthalpies of TiB_6, defined by Eqs. (1)–(4), are calculated with respect to distinct reference phases (including elemental Ti/B, TiB, Ti_3B_4, and TiB_2) to comprehensively evaluate its thermodynamic stability.

$$\Delta H_{f1} = H_{TiB_6} - (H_{Ti} + 6H_B), \tag{1}$$

$$\Delta H_{f2} = H_{TiB_6} - (H_{TiB} + 5H_B), \tag{2}$$

$$\Delta H_{f3} = H_{TiB_6} - (H_{Ti_3B_4} + 14H_B)/3, \tag{3}$$

$$\Delta H_{f4} = H_{TiB_6} - (H_{TiB_2} + 4H_B). \tag{4}$$

The $P6/mmm$-Ti, $P6/mmm$-TiB_2,[50] α-B, and γ-B[54] are chosen as reference phases. As illustrated in Fig. 4, various reaction pathways were identified based on different synthesis conditions. Here, taking the α-*Amm*2 and β-*Amm*2 phases of TiB_6 as examples, the fourth reaction pathway involving TiB_2 as a precursor is not accessible within the pressure range of 0–100 GPa. In contrast, the first and second pathways with negative formation enthalpies are thermodynamically favorable. The third pathway becomes accessible under conditions of 6.8 GPa and 7.8 GPa for the two structures, respectively. These results indicate that the five predicted TiB_6 phases are thermodynamically stable at ambient conditions.

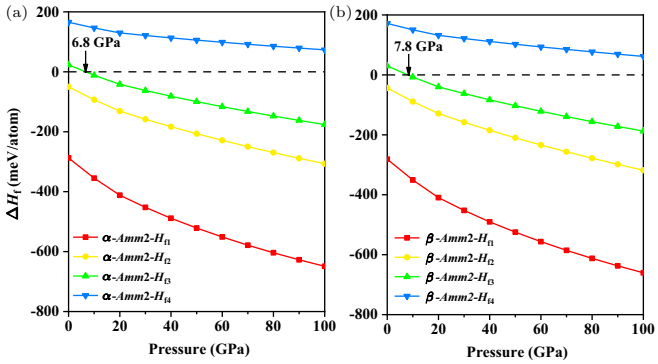


Fig. 4. Calculated formation enthalpies (ΔH_f) as a function of pressure. (a) α-*Amm*2-TiB_6, (b) β-*Amm*2-TiB_6.

3.3. Mechanical property

Besides evaluating thermodynamic and dynamical stability, we additionally assessed the mechanical stability of the predicted structures. The mechanical stability of the phases is determined via the analysis of elastic constants (C_{ij}).[55] For the orthorhombic and monoclinic crystal systems considered in this study, the mechanical stability criteria require that the elastic constants satisfy specific constraints. Orthorhombic lattices must adhere to the following conditions.

For orthorhombic crystals,[56]

$$C_{11} > 0,\ C_{22} > 0,\ C_{33} > 0,\ C_{44} > 0,\ C_{55} > 0,\ C_{66} > 0,$$
$$[C_{11} + C_{22} + C_{33} + 2(C_{12} + C_{13} + C_{23})] > 0,$$
$$(C_{11} + C_{22} - 2C_{12}) > 0,\ (C_{11} + C_{33} - 2C_{13}) > 0,$$
$$(C_{22} + C_{33} - 2C_{23}) > 0.$$

For monoclinic crystals,[56]

$$C_{11} > 0,\ C_{22} > 0,\ C_{33} > 0,\ C_{44} > 0,\ C_{55} > 0,\ C_{66} > 0,$$
$$[C_{11} + C_{22} + C_{33} + 2(C_{12} + C_{13} + C_{23})] > 0,$$
$$\left(C_{33}C_{55} - C_{35}^2\right) > 0,\ \left(C_{44}C_{66} - C_{46}^2\right) > 0,$$
$$(C_{22} + C_{33} - 2C_{23}) > 0,$$
$$\left[C_{22}\left(C_{33}C_{55} - C_{35}^2\right) + 2C_{23}C_{25}C_{35} - C_{23}^2C_{55} - C_{25}^2C_{33}\right] > 0,$$
$$2\Big[C_{15}C_{25}(C_{33}C_{12} - C_{13}C_{23}) + C_{15}C_{35}(C_{22}C_{13} - C_{12}C_{23})$$
$$+C_{25}C_{35}(C_{11}C_{23} - C_{12}C_{13})\Big] - \Big[C_{15}^2\left(C_{22}C_{33} - C_{23}^2\right)$$
$$+C_{25}^2\left(C_{11}C_{33} - C_{13}^2\right) + C_{35}^2\left(C_{11}C_{22} - C_{12}^2\right)\Big]$$
$$+C_{55}\Big(C_{11}C_{22}C_{33} - C_{11}C_{23}^2 - C_{22}C_{13}^2$$
$$-C_{33}C_{12}^2 + 2C_{12}C_{13}C_{23}\Big) > 0.$$

As presented in Table 1, the elastic constants of all TiB_6 structures under investigation satisfy the mechanical stability criteria, thereby confirming their mechanical stability under ambient pressure conditions. To provide a reference for comparative analysis with the newly predicted structures, the corresponding data of previously reported $C2/m$-Ti_2B_5,[36] *Amm*2-TiB_3,[33] $C2/m$-TiB_3,[33] *Amm*2-TaB_6,[15] and *Amm*2-HfB_6[18] at 0 GPa were also listed in Table 1. All structures exhibit significantly large values of C_{11}, C_{22}, and C_{33}, indicating that compression along the *a*-, *b*-, and *c*-axes is difficult, respectively. Of particular note is α-*Amm*2-TiB_6, where $C_{11} = 694$ GPa and $C_{22} = 663$ GPa, indicating its extreme incompressibility along the *a*- and *b*-axes. Collectively, all TiB_6 phases demonstrate thermodynamic, dynamical, and mechanical stability at 0 GPa.

The Voigt–Reuss–Hill approximation was employed to derive the bulk modulus (B) and shear modulus (G) from the elastic constants. Young's modulus (E) and Poisson's ratio (ν) were subsequently calculated using the standard relations $E = 9BG/(3B + G)$ and $\nu = (3B - 2G)/(6B + 2G)$, respectively. These parameters, including B, G, E, and ν, are systematically tabulated in Table 2. The estimated hardness of the five TiB_6 compounds was evaluated using Chen's model: $H_V = (2k^2G)^{0.585} - 3$ and Tian's model: $H_V = 0.92k^{1.137}G^{0.708} - 3$,

Table 1. Calculated elastic constants C_{ij} (GPa) of Ti_2B_5, TiB_3, TaB_6, HfB_6, and TiB_6 at 0 GPa. The elastic properties of previously reported transition-metal borides are included for comparison.

Structure	Ref.	C_{11}	C_{22}	C_{33}	C_{44}	C_{55}	C_{66}	C_{12}	C_{13}	C_{23}	C_{15}	C_{25}	C_{35}	C_{46}
$C2/m$-Ti_2B_5	Present	657	652	483	244	254	292	61	93	86	−7	1	19	2
	Ref. [36]	651	650	476	217	252	281	66	95	90				
$Amm2$-TiB_3	Present	498	668	653	289	263	245	78	88	62	–	–	–	–
$C2/m$−TiB_3	Present	662	650	517	231	250	288	61	82	74	−15	1	−37	2
$Amm2$-TaB_6	Present	640	674	697	277	231	221	87	73	90	–	–	–	–
	Ref. [15]	641	651	688	252	239	188	87	68	97	–	–	–	–
$Amm2$-HfB_6	Present	562	660	615	274	276	273	62	90	56	–	–	–	–
	Ref. [18]	546	638	619	260	264	222	85	90	58	–	–	–	–
α-$Amm2$-TiB_6	Present	694	663	577	275	227	284	54	41	70	–	–	–	–
β-$Amm2$-TiB_6	Present	691	620	544	272	233	272	54	66	87	–	–	–	–
$P2/m$−TiB_6	Present	486	562	666	251	256	222	75	94	66	59	−12	63	13
α-$P2_1/m$−TiB_6	Present	623	593	545	225	264	224	47	88	59	−59	9	−74	−12
β-$P2_1/m$-TiB_6	Present	520	604	711	284	242	256	100	67	74	13	1	−14	2

Table 2. Calculated shear modulus G (GPa), Young's modulus E (GPa), G/B ratio, Poisson's ratio ν, and Vickers hardness H_V (GPa) of TiB_6, TiB_3, and HfB_6 at 0 GPa. The elastic properties of previously reported transition-metal borides are included for comparison.

Structure	Ref.	G	E	G/B	ν	H_v^{Chen}	H_v^{Tian}
$C2/m$-Ti_2B_5	Present	259	578	1.03	0.115	–	48.8
	Ref. [36]	249	561	0.99	0.127	–	46.9
$Amm2$-TiB_3	Present	264	587	1.04	0.111	52.2	50.3
	Ref. [33]	268	599	1.03	0.133	51.6	49.9
$C2/m$-TiB_3	Present	259	578	1.03	0.114	50.9	49.1
	Ref. [33]	254	570	1.01	0.128	48.4	47.2
$Amm2$-TaB_6	Present	261	597	0.93	0.143	–	43.9
	Ref. [15]	246	568	0.89	0.156	–	40.8
$Amm2$-HfB_6	Present	264	587	1.05	0.109	52.7	50.8
	Ref. [18]	253	568	1.00	0.124	48.1	46.5
α-$Amm2$-TiB_6	Present	274	602	1.09	0.100	55.9	53.9
β-$Amm2$-TiB_6	Present	264	587	1.05	0.112	52.1	50.3
$P2/m$-TiB_6	Present	488	542	1.24	0.122	47.0	45.2
α-$P2_1/m$-TiB_6	Present	480	545	1.23	0.115	49.0	47.0
β-$P2_1/m$-TiB_6	Present	261	585	1.02	0.120	50.5	48.4

where Pugh's ratio is denoted by k and G is the shear modulus. The computed hardness values are also listed in Table 2.

Significantly, the orthorhombic α-$Amm2$-TiB_6 phase demonstrates exceptional mechanical performance, achieving a theoretical hardness of 55.9 GPa. This value not only exceeds previous records within the Ti–B system, but also surpasses the hardness of previously reported transition-metal boride compounds. These findings provide important theoretical insights for the rational design of novel transition-metal boride superhard materials. Furthermore, the calculated shear modulus (G) and Vickers hardness of $C2/m$-Ti_2B_5,[36] $Amm2$-TiB_3,[33] $C2/m$-TiB_3,[33] $Amm2$-TaB_6,[15] and $Amm2$-HfB_6[18] at ambient pressure were also listed in Table 2, together with comparative data from previous studies. These results are consistent with previous theoretical predictions for transition-metal borides, thus validating the reliability of the computational approach.

Elastic anisotropy in crystals exhibits orientation dependence. To visually demonstrate elastic anisotropy, the variations of the bulk modulus and Young's modulus with crystal orientation were investigated.[57,58] For isotropic crystals, three-dimensional (3D) plots of elastic parameters should exhibit spherical symmetry, and any deviation from sphericity indicates elastic anisotropy. Taking the α-$Amm2$ and β-$Amm2$ phases of TiB_6 as examples, Figs. 5(a) and 5(c) display the 3D plots of the bulk modulus and Young's modulus of α-$Amm2$-TiB_6. The 3D plots of α-$Amm2$-TiB_6 are not spherical. More pronounced anisotropy is observed in Young's modulus compared with the bulk modulus. The calculated ratios of $B_{\max}/B_{\min}$ and $E_{\max}/E_{\min}$ are 1.195 and 1.295, respectively, indicating anisotropic elastic behavior. Figures 5(b) and 5(d) display two-dimensional (2D) projections of bulk modulus and Young's modulus for α-$Amm2$-TiB_6 on the xy, xz, and yz planes. These projections demonstrate the directional dependence of elastic properties, revealing the anisotropy of α-$Amm2$-TiB_6. In particular, the 2D projection of the bulk

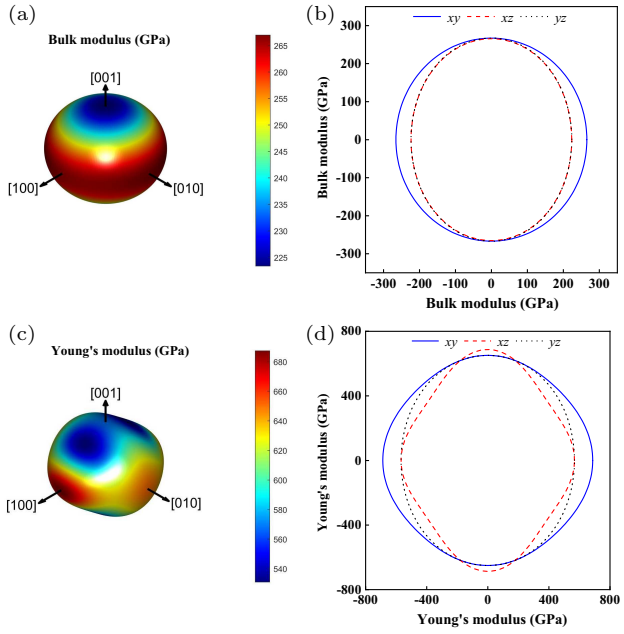


Fig. 5. Calculated 3D surfaces and two-dimensional (2D) projections of the bulk modulus and Young's modulus for α-$Amm2$-TiB_6.

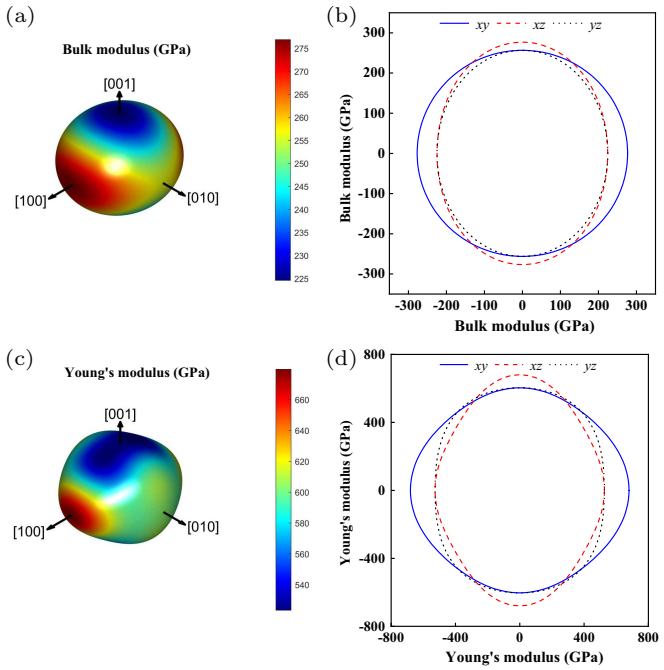


Fig. 6. Calculated 3D surfaces and 2D projections of the bulk modulus and Young's modulus for β-*Amm*2-TiB_6.

modulus on the *xy* plane is nearly circular. In contrast, elastic anisotropy is significant on the *xz* and *yz* planes, where the projection curves are noncircular. Likewise, the elastic anisotropy of β-*Amm*2-TiB_6 is investigated through 3D renderings of bulk modulus and Young's modulus, illustrated in Figs. 6(a) and 6(c). Specifically, Young's modulus exhibits pronounced anisotropy. This feature originates from the deviation of its 3D surface from spherical symmetry, indicating direction-dependent deformation resistance. The 3D plots of β-*Amm*2-TiB_6 are not spherical. Again, compared with the bulk modulus, Young's modulus shows more obvious anisotropy. The calculated ratios of B_{max}/B_{min} and E_{max}/E_{min} are 1.233 and 1.299, respectively, indicating anisotropic elastic behavior. The 2D projections in Figs. 6(b) and 6(d) further support this conclusion. Since α-*Amm*2-TiB_6 and β-*Amm*2-TiB_6 have similar structures, differing only in the number of B layers, they exhibit nearly identical anisotropy. 3D plots and 2D projections of bulk modulus and Young's modulus for the three monoclinic structures are illustrated in Figs. S4–S6. From the above analysis, the following conclusions can be drawn. (I) Elastic isotropy is approximately observed for the bulk modulus in the *xy* plane. (II) The anisotropy of Young's modulus in the *xy* plane is weaker than that in the *xz* and *yz* planes. (III) Both materials exhibit relatively strong anisotropy in Young's modulus.

3.4. Electronic structure

In order to further investigate the electronic properties of TiB_6 phases at ambient pressure, we performed a comprehensive analysis of their band structures, as illustrated in Fig. 7. The results show that all TiB_6 phases exhibit multiple electronic bands crossing the Fermi level, accompanied by a finite density of states at the Fermi energy. These features confirm the metallic behavior of these borides and suggest potential electrical conductivity.

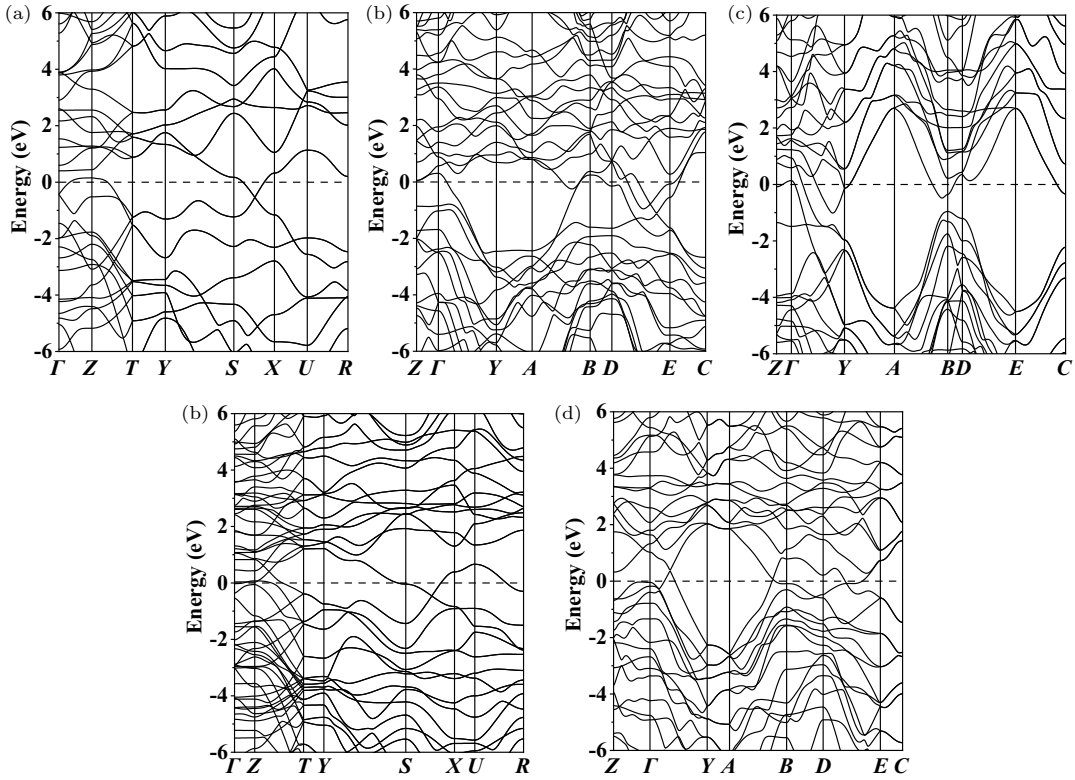


Fig. 7. Electronic band structures and densities of states of TiB_6. (a) α-*Amm*2, (b) β-*Amm*2, (c) *P*2/*m*, (d) α-*P*2$_1$/*m*, and (e) β-*P*2$_1$/*m* at 0 GPa. The horizontal dashed line represents the Fermi level.

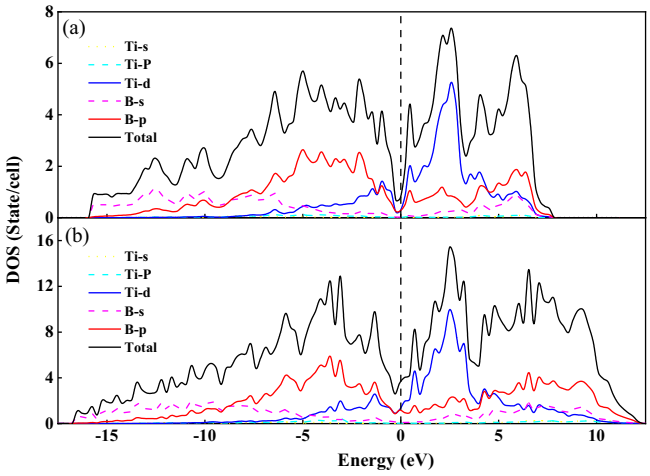


Fig. 8. Calculated PDOS of TiB_6. (a) α-*Amm*2 and (b) β-*Amm*2 at 0 GPa.

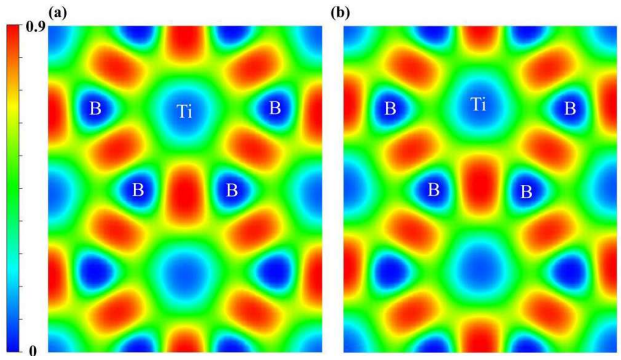


Fig. 9. ELF contour maps of α-*Amm*2-TiB_6 in the (001) plane and β-*Amm*2-TiB_6 in the ($\bar{1}$00) plane at 0 GPa.

To gain a better understanding of the electronic properties of TiB_6, we calculated the projected densities of states (PDOS) of the α-*Amm*2 and β-*Amm*2 phases, as shown in Fig. 8. The PDOS analysis reveals that the Ti-3d and B-2p orbitals play dominant roles in their metallicity. The metallic behavior in all investigated compounds originates from the non-zero density of states at the Fermi level. States below -5 eV are predominantly derived from B-2s and B-2p orbitals, while contributions in the -5 eV to 0 eV range mainly arise from hybridization between B-2p and Ti-3d states. Notably, the B-2s states are partially hybridized with B-2p states, leading to strong localization within the boron sublattice. This hybridization facilitates the formation of robust covalent B–B bonds, which significantly enhance deformation resistance and intrinsic hardness of TiB_6. In addition, distinct orbital hybridization occurs between Ti-3d states and B-2s or B-2p states. This localized Ti–B orbital hybridization drives the formation of directional Ti–B bonds. Consequently, the exceptional hardness of TiB_6 arises synergistically from two key factors: the covalent bonding network within the B–B framework and the directional covalent bonding between Ti and B atoms. This analysis is consistent with fundamental principles of electronic structure in transition-metal borides, where hybridization between metal d orbitals and light-element p orbitals governs macroscopic mechanical properties. The PDOS results for the monoclinic phases are presented in Supplementary Fig. S3.

To gain deeper insights into the bonding characteristics of TiB_6, we performed electronic localization function (ELF) calculations to analyze electron pairing. In Fig. 9, the ELF contour distributions of α-*Amm*2-TiB_6 on the (001) plane are presented, while those for β-*Amm*2-TiB_6 are shown on the ($\bar{1}$00) plane at 0 GPa, with additional monoclinic data provided in Fig. S2. The analysis demonstrates that significant electron localization exists between neighboring B atoms. Such covalent bonding features directly contribute to the enhanced mechanical hardness and structural integrity of the TiB_6 system, as evidenced by the robust electron localization patterns. These results establish the critical role of B–B covalent bonding in determining the mechanical properties.

4. Conclusion

In conclusion, to investigate novel transition-metal boride superhard materials, we employed the CALYPSO algorithm combined with first-principles calculations to predict the crystal structures of TiB_6. Our analysis yielded five stable phases: α-*Amm*2, β-*Amm*2, $P2/m$, α-$P2_1/m$, and β-$P2_1/m$. Notably, the α-*Amm*2-TiB_6 phase exhibits exceptional hardness. According to Chen's model, its Vickers hardness is estimated to reach 55.9 GPa, indicating its potential as a superhard material. Compared with previously reported TiB compounds, the newly proposed α-*Amm*2-TiB_6 is among the hardest known phases in the Ti–B system. The stability of all explored TiB_6 compounds, including dynamical, thermodynamic, and mechanical stability, was confirmed through phonon spectra, formation enthalpies, and elastic constant calculations.

Acknowledgments

This work was supported by the Scientific and Technological Research Project of the Jilin Provincial Education Department (Grant No. JJKH20240077KJ) and the Jilin Provincial Science and Technology Development Joint Fund Project (Grant No. YDZJ202201ZYTS581).

References

[1] Sung C M and Sung M 1996 *Mater. Chem. Phys.* **43** 1
[2] Haines J, Léger J and Bocquillon G 2001 *Annu. Rev. Mater. Res.* **31** 1
[3] Kaner R B, Gilman J J and Tolbert S H 2005 *Science* **308** 1268
[4] Dong J, Yao Z, Yao M, Li R, Hu K, Zhu L, Wang Y, Sun H, Sundqvist B, Yang K and Liu B 2020 *Phys. Rev. Lett.* **124** 065701
[5] Liu H, Li Q, Zhu L and Ma Y 2011 *Phys. Lett. A* **375** 771
[6] Zhang M, Liu H, Li Q, Gao B, Wang Y, Li H, Chen C and Ma Y 2015 *Phys. Rev. Lett.* **114** 015502
[7] Wentorf R H 1957 *J. Chem. Phys.* **26** 956
[8] Du J and Li X 2020 *J. Alloys Compd.* **815** 152324
[9] Akopov G, Pangilinan L E, Mohammadi R and Kaner R B 2018 *APL Mater.* **6** 070901
[10] Yeung M T, Mohammadi R and Kaner R B 2016 *Annu. Rev. Mater. Res.* **46** 465

[11] Chung H Y, Weinberger M B, Levine J B, Kavner A, Yang J M, Tolbert S H and Kaner R B 2007 *Science* **316** 436
[12] Niu H, Wang J, Chen X Q, Li D, Li Y, Lazar P, Podloucky R and Kolmogorov A N 2012 *Phys. Rev. B* **85** 144116
[13] Li X and Peng F 2019 *Phys. Chem. Chem. Phys.* **21** 15609
[14] Lin H S, Wang C Y, Djouadi M A, Kuang T C and Dong H F 2023 *J. Mater. Sci.* **58** 1139
[15] Zhang G, Bai T, Feng G and He J 2024 *Mater. Today Commun.* **41** 110318
[16] Mohn P 1988 *J. Phys. C Solid State Phys.* **21** 2841
[17] Ding L P, Tiandong Y H, Shao P, Tang Y, Zhao Z L and Lu H 2021 *J. Phys. Chem. Lett.* **12** 5423
[18] Xie C, Zhang Q, Zakaryan H A, Wan H, Liu N, Kvashnin A G and Oganov A R 2019 *J. Appl. Phys.* **125** 205109
[19] Huang L H, Zhao Y R, Zhang G T, Zhang M G, Li P Y and Hu Y F 2019 *Mol. Phys.* **117** 547
[20] Wei S, Li D, Lv Y, Liu Z, Tian F, Duan D, Liu B and Cui T 2016 *J. Alloys Compd.* **688** 1101
[21] Ji Z W, Hu C H, Wang D H, Zhong Y, Yang J, Zhang W Q and Zhou H Y 2012 *Acta Mater.* **60** 4208
[22] Zhang X, Zhao E and Wu Z 2015 *J. Alloys Compd.* **632** 37
[23] Zhang M, Wang H, Wang H, Zhang X, Iitaka T and Ma Y 2010 *Inorg. Chem.* **49** 6859
[24] Ding L P, Shao P, Zhang F H, Lu C, Ding L, Ning S Y and Huang X F 2016 *Inorg. Chem.* **55** 7033
[25] Zhang M, Lu M, Du Y, Gao L, Lu C and Liu H 2014 *J. Chem. Phys.* **140** 174505
[26] Knappschneider A, Litterscheid C, Dzivenko D, Kurzman J A, Seshadri R, Wagner N, Beck J, Riedel R and Albert B 2013 *Inorg. Chem.* **52** 540
[27] Li X, Tao Y and Peng F 2016 *J. Alloys Compd.* **687** 579
[28] Li Q, Zhou D, Zheng W, Ma Y and Chen C 2015 *Phys. Rev. Lett.* **115** 185502
[29] Decker B F and Kasper J S 1954 *Acta Crystallogr.* **7** 77
[30] Norton J T, Blumenthal H and Sindeband S J 1949 *JOM* **1** 749
[31] Cao K, Shi G Y, Liu T T, Li X, Li J F, Wang X L, Su Y H, Zhang C and Jiang H 2023 *Vacuum* **217** 112582
[32] Li P, Zhou R and Zeng X C 2015 *ACS Appl. Mater. Interfaces* **7** 15607
[33] Chen M R, Dou X L, Song T, Yan Z P and Sun X W 2024 *Results Phys.* **61** 107779
[34] Pan Y 2023 *Phys. Chem. Chem. Phys.* **25** 24417
[35] Pan Y and Jia Y 2019 *J. Mater. Res.* **34** 3554
[36] Zhang G, Song Y, Bai T, Zhang M and Liu T 2023 *Comput. Mater. Sci.* **228** 112379
[37] Kresse G and Furthmüller J 1996 *Phys. Rev. B* **54** 11169
[38] Kohn W and Sham L J 1965 *Phys. Rev.* **140** A1133
[39] Wang Y, Lv J, Zhu L and Ma Y 2010 *Phys. Rev. B* **82** 094116
[40] Wang Y, Lv J, Zhu L and Ma Y 2012 *Comput. Phys. Commun.* **183** 2063
[41] Perdew J P, Burke K and Ernzerhof M 1996 *Phys. Rev. Lett.* **77** 3865
[42] Perdew J P and Wang Y 1992 *Phys. Rev. B* **45** 13244
[43] Kresse G and Joubert D 1999 *Phys. Rev. B* **59** 1758
[44] Blöchl P E 1994 *Phys. Rev. B* **50** 17953
[45] Monkhorst H J and Pack J D 1976 *Phys. Rev. B* **13** 5188
[46] Togo A, Oba F and Tanaka I 2008 *Phys. Rev. B* **78** 134106
[47] Chen X Q, Niu H, Li D and Li Y 2011 *Intermetallics* **19** 1275
[48] Tian Y, Xu B and Zhao Z 2012 *Int. J. Refract. Metals Hard Mater.* **33** 93
[49] Šimůnek A 2009 *Phys. Rev. B* **80** 060103
[50] Deligoz E, Colakoglu K and Ciftci Y O 2009 *Solid State Commun.* **149** 1843
[51] Liu A, Cheng X, Wang X, Zou Y and Zhang M 2023 *Phys. Chem. Chem. Phys.* **25** 20837
[52] Liu J, Liu A, Wang Y, Gao L, Luo X and Zhang M 2025 *Chin. Phys. B* **34** 046201
[53] Wang X F, Wang Y X, Wang Z, Zhang Y X and Gu J B 2024 *Chin. Phys. B* **33** 126103
[54] Oganov A R, Chen J, Gatti C, Ma Y, Ma Y, Glass C W, Liu Z, Yu T, Kurakevych O O and Solozhenko V L 2009 *Nature* **457** 863
[55] Ivanovskii A L 2012 *Prog. Mater. Sci.* **57** 184
[56] Wu Z J, Zhao E J, Xiang H P, Hao X F, Liu X J and Meng J 2007 *Phys. Rev. B* **76** 059904
[57] Yan H, Zhang W, Chen L, Zhang Y, Wang H, Zhang M and Wei Q 2025 *Phys. Chem. Chem. Phys.* **27** 6134
[58] Liao M, Liu Y, Cui P, Qu N, Zhou F, Yang D, Han T, Lai Z and Zhu J 2020 *Comput. Mater. Sci.* **172** 109289